

Research Article

Stiffness Modeling of Tooth Interior Fatigue and Tooth Flank Fracture and Their Fault Characteristics in Electromechanical Coupling Systems

Lin Han ¹, Dianrui Wang,¹ Muhammad Anwar Jan,¹ and Fuchun Yang ^{1,2}

¹Key Laboratory of High Efficiency and Clean Mechanical Manufacture of MOE, School of Mechanical Engineering, Shandong University, Jinan 250061, China

²National Demonstration Center for Experimental Mechanical Engineering Education (Shandong University), Jinan 250061, China

Correspondence should be addressed to Fuchun Yang; fuchunyang@sdu.edu.cn

Received 28 August 2023; Revised 19 December 2023; Accepted 30 January 2024; Published 15 February 2024

Academic Editor: Zhipeng Zhao

Copyright © 2024 Lin Han et al. This is an open access article distributed under the Creative Commons Attribution License, which permits unrestricted use, distribution, and reproduction in any medium, provided the original work is properly cited.

Tooth flank fracture (TFF) and tooth interior fatigue fracture (TIFF) usually occur on case-hardened gears in electromechanical coupling systems, both starting from the core caused by metal fatigue. The cracks propagate rapidly compared with the total life of a gear, so that it is necessary to detect and identify the faults in time when they take place in order to avoid danger. In this paper, the time-varying mesh stiffness model of two types of faults is established by the potential energy method and validating by the finite element method. Based on the stiffness model, the influence of faults on the electromechanical system and their fault characteristics are analyzed, which provides a theoretical basis for the health detection of electromechanical coupling systems. The results indicate that in the early stage of the three faults, i.e., tooth root fracture, tooth interior fatigue fracture, and tooth flank fracture, it is hard to discriminate the faults. But after the second stage, the faults can be distinguished by the vibration amplitude, frequency band components, and phase diagrams. The TFF can be discerned into different stages by frequency domains and phase diagrams. When the fracture occurs completely, three faults can be easily distinguished by the time domain and phase diagram. In the frequency domain, the TRF can also be distinguished from the other two faults by referring to the sideband component near the meshing frequency.

1. Introduction

In modern industry, electromechanical gear systems are widely used in various scenarios, such as engineering machinery, trains, vehicles, and vessels. Among them, gear plays an important role. Once a failure occurs, it will result in equipment damage and great economic losses. Gear faults can be classified into pitting, scuffing, wearing, cracks, and fractures [1]. The impact of fracture failure is the greatest. Fractures include tooth root fracture (TRF), tooth flank fracture (TFF), and tooth interior fatigue fracture (TIFF) [2, 3], in which the latter two are the fault types that are easy to occur in case-hardened gears that have attracted attention in recent years. When the crack or fracture occurs, it will change the time-varying meshing stiffness of the gear pair

and cause the periodic impact in the gear set, which will have a nonnegligible impact on the reliability, vibration, and noise of the system. Compared with tooth root fractures, TFF and TIFF faults are more difficult to detect after a fault occurs because the crack initiation point is inside the gear.

For stiffness modeling of healthy and faulty gear tooth, Yang and Lin [4] considered the gear teeth as a variable-section cantilever beam fixed on the base circle, and the potential energy method is used to calculate the time-varying mesh stiffness of the gear tooth. Sainsot et al. [5] proposed a gear body deformation correction formula considering the ring structure of the actual gear. On this basis, Chen and Shao [6] proposed a calculation model of time-varying meshing stiffness considering gear body deformation. Liang et al. [7] used the potential energy method

to model the meshing stiffness of planetary gear set under root crack failure, derived the analytic equation of meshing stiffness, and established the crack growth model under tooth root crack. Mohammed et al. [8] studied the time-varying meshing stiffness of gear pairs under three kinds of root cracks based on the depth and path of the crack. Doğan et al. [9] studied the influence of rim thickness and pressure angle on root crack propagation and determined the direction of crack propagation under different rim thicknesses and pressure angles. Wang et al. [10] studied the relationship between the meshing coupling behavior of spur gear and root crack propagation and established finite element models for different fault stages of root crack. Wu et al. [11] proposed a meshing stiffness calculation model under four different crack depths under the root fracture based on the potential energy method. Boiadjev et al. [3] mainly conducts an experimental study on fatigue fracture crack propagation and the concrete path was given. Schneider et al. [12] established a phase field model for tooth flank fracture under the condition of the constant driving torque and studied the starting position and propagation path of the crack. Al et al. [13] established a three-dimensional contact model of tooth flank fracture and interior fatigue fracture by using SMT's MASTA software and obtained the load boundary conditions of the failure. MackAldener et al. [2] conducted three-dimensional modeling of the interior fatigue fracture of gear and obtained the crack propagation path under the fault.

For electromechanical coupling, dynamic modeling, and fault characteristics, Yi et al. [14] established an induction motor model and a dynamic model of multistage gear transmission and then analyzed the influence of the electromagnetic characteristics on the dynamic response of the transmission system. Bai et al. [15] analyzed the dynamic characteristics of the electromechanical model by combining the nonlinear permeance network model of the squirrel-cage motor and the lateral-torsional coupled dynamic model of the planetary gear system. Shu et al. [16] proposed an electromechanical coupling dynamic model that can reflect the multimotor driving system under time-varying load and speed conditions. Kahraman [17] established the pure torsional dynamics model of a single-stage planetary gear train and studied the natural vibration characteristics of the system. Lin and Parker [18] established a dynamics model considering the torsional and translational degrees of freedom of all components in a planetary gear system and studied the natural frequencies and vibration modes of the system. Liu et al. [19] developed a dynamic gear model by incorporating both the driving speed and the drag torque as external excitation sources and then proposed a solution method based on adaptive selection of the time-step method and the time-step reduced method to optimize the calculation process. Wang et al. [20] considered the impact of the inverter on the electromechanical coupling system, constructed a variable-frequency drive electromechanical coupling model, and studied the dynamic characteristics of motor speed regulation. Han et al. [21] established an electromechanical coupling dynamic model that includes a pair of fixed-axis gears and studied the impact of system parameters on vibration characteristics. Chen and Shao [6]

proposed an analytical model of meshing stiffness variation based on the potential energy method, and a dynamic lumped parameter model of a spur gearbox system comprising six degrees of freedom is established. The dynamic response of cracked gear was studied by statistical index root mean square (RMS) and kurtosis. Mohammed et al. [22] established a gear dynamics model of 12 degrees of freedom and calculated the gear time-varying mesh stiffness under different stages of root cracks. Liu et al. [23] proposed a new nonlinear dynamic model for spur gear systems, considering dynamic force increment, together with the effect of velocity-dependent mesh stiffness, and obtained the dynamic response of the system. Abouel-seoud et al. [24] established a dynamic gearbox model of wind turbines containing spalling faults and analyzed fault characteristics through the time domain and frequency domain of vibration signals. Ma and Chen [25] established a dynamic model of gear systems including root cracks and spalling faults. Using time domain, phase trajectory, Poincare section, spectrum analysis, and other methods, the difference and comparison of vibration signals under the two failures were discussed.

In previous research, the stiffness models and fault characteristics of tooth root fractures are studied. However, research is focused on the crack propagation and lacks stiffness calculation models for tooth flank fracture and tooth interior fatigue fracture caused by interior cracks. Contributions in this paper are as follows: (1) the time-varying mesh stiffness calculation models of tooth flank fracture and tooth interior fatigue fracture are established, and the finite element method is used to validate the established model, and (2) the coupling dynamic model of the power-motor-gear electromechanical system with different gear faults is established, and the fault characteristics of tooth flank fracture and tooth interior fatigue fracture in the coupling system are studied.

2. Stiffness Modeling of Tooth Flank Fracture and Tooth Interior Fatigue Fracture

For the gear with healthy teeth, tooth flank fracture, and tooth interior fatigue fracture, the improved potential energy method (PEM) considering the gear body is used to calculate the time-varying meshing stiffness, and the results are verified by the finite element method (FEM). The schematic diagram of the calculation model is shown in Figure 1.

In Figure 1, R_r and R_b are the radii of the root circle and the base circle; d_1 is the length of a simplified straight line intersecting the root and base circles on the tooth profile; α_2 represents the half tooth angle on the base circle; while α_3 describes the approximated half tooth angle on the root circle; x is the distance between any position and the root of the gear; α and h_x are the engagement angle and height of the section, where the distance to the tooth root is x ; d is the distance from the contact point to the root of the tooth; α_1 and h are the engagement angle and height of the section at the contact point; F is the meshing force; and F_a and F_b are the horizontal and vertical components.

Considering the deformation of gears under load, the energy of gears in meshing can be divided into Hertz contact

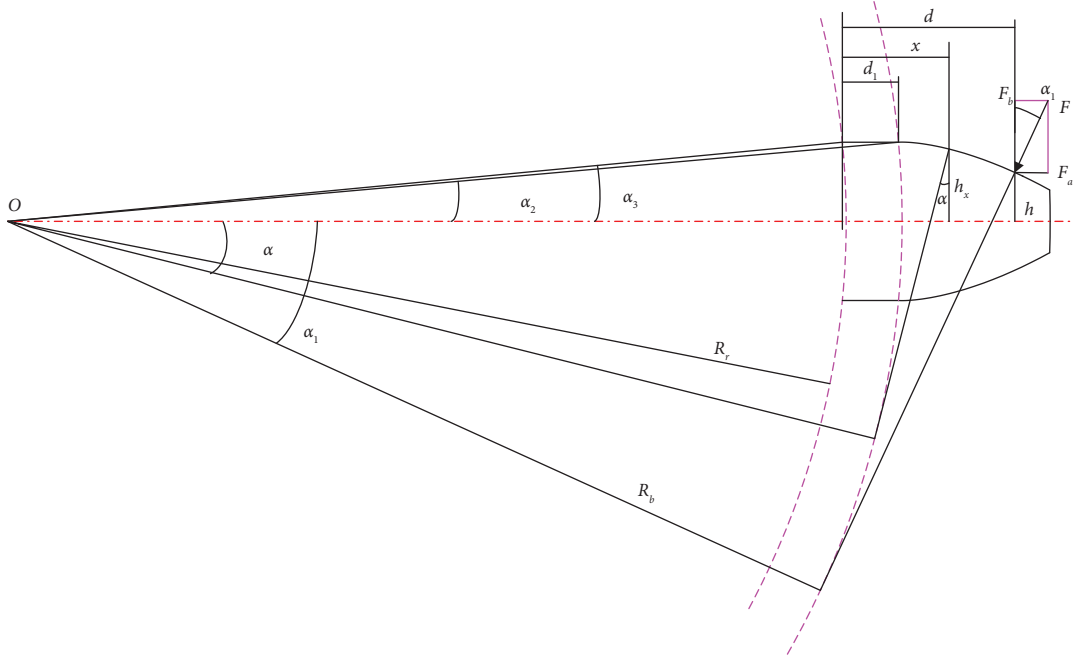


FIGURE 1: Cantilever beam model of a gear tooth.

energy U_h , bending energy U_b , axial compression energy U_a , shear energy U_s , and gear body energy U_f .

$$\begin{aligned} U_h &= \frac{F^2}{2k_h}, \\ U_b &= \frac{F^2}{2k_b}, \\ U_a &= \frac{F^2}{2k_a}, \\ U_s &= \frac{F^2}{2k_s}, \\ U_f &= \frac{F^2}{2k_f}. \end{aligned} \quad (1)$$

According to Hertz's law, the Hertz contact stiffness is a constant along the meshing line, and its value is independent of the meshing contact position as follows:

$$k_h = \frac{\pi EL}{4(1-\nu^2)}, \quad (2)$$

where E and ν , respectively, represent the elastic modulus and Poisson's ratio of the material, which are determined by the material of the gear teeth, and L is the width of the gear tooth. Therefore, the Hertz contact stiffness is theoretically constant.

Based on beam theory, equations (3)–(5) can be obtained as follows:

$$\frac{1}{k_b} = \int_0^d \frac{[\cos \alpha_1 (d-x) - \sin \alpha_1 h]^2}{EI_x} dx, \quad (3)$$

$$\frac{1}{k_s} = \int_0^d \frac{1.2 (\cos \alpha_1)^2}{GA_x} dx, \quad (4)$$

$$\frac{1}{k_a} = \int_0^d \frac{(\sin \alpha_1)^2}{EA_x} dx, \quad (5)$$

where k_b , k_a , and k_s represent the flexural stiffness, axial compression stiffness, and shear stiffness, respectively; E and G are Young's modulus and shear modulus; A_x and I_x are the corresponding area and moment of inertia when the distance from the tooth root is x ; h , d , h_x , A_x , and I_x can be expressed as

$$\begin{aligned} h &= R_b [(\alpha_1 + \alpha_2) \cos \alpha_1 - \sin \alpha_1], \\ d &= R_b [(\alpha_1 + \alpha_2) \sin \alpha_1 + \cos \alpha_1] - R_r \cos \alpha_3, \\ h_x &= \begin{cases} R_b \sin \alpha_2, & \text{if } 0 < x < d_1, \\ R_b [(\alpha_2 - \alpha) \cos \alpha + \sin \alpha], & \text{if } d_1 < x < d, \end{cases} \end{aligned} \quad (6)$$

$$A_x = 2h_x L,$$

$$I_x = \frac{1}{12} (2h_x)^3 L.$$

It can be seen from the above equation that for gears with involute tooth profiles, the values of flexural stiffness, shear stiffness, and axial compression stiffness are related to α_1 , d ,

h , A_x , and I_x but these parameters are functions of α_1 , so they all depend on the meshing position.

The gear body stiffness calculation method of gears selected in this paper [5] is as follows:

$$\frac{1}{k_f} = \frac{\cos^2 \alpha_1}{EL} \left[L^* \left(\frac{u_f}{s_f} \right)^2 + M^* \left(\frac{u_f}{s_f} \right) + P^* (1 + Q^* \tan^2 \alpha_1) \right], \quad (7)$$

where s_f is the thickness at the root of the gear and u_f is the distance from the intersection between the normal of the gear meshing point and the center line of the gear tooth to the root of the gear, r_f and r_{int} are, respectively, the radii of the root circle and the radius of the shaft hole (as shown in

Figure 2); and L^* , M^* , P^* , and Q^* are the calculation coefficients of gear body stiffness, which are related to the number of teeth and radius of shaft holes. The expression is shown in the following equation:

$$X^* = \frac{A}{\theta_f^2} + Bh_f^2 + \frac{Ch_f}{\theta_f} + \frac{D}{\theta_f} + Eh_f + F, \quad (8)$$

where h_f represents the ratio of the radius of the gear hole to the radius of the root circle. The values of A , B , C , D , E , and F are shown in Table 1.

Hertz stiffness, bending stiffness, shear stiffness, axial compression stiffness, and gear body stiffness are integrated to form the synthesizing stiffness during gear meshing as

$$k_t = \frac{1}{1/k_h + 1/k_{b1} + 1/k_{s1} + 1/k_{a1} + 1/k_{f1} + 1/k_{b2} + 1/k_{s2} + 1/k_{a2} + 1/k_{f2}}. \quad (9)$$

The gear parameters used in this paper are shown in Table 2.

Considering the contact ratio, the single-tooth meshing stiffness is superimposed with the single-tooth meshing stiffness of the previous and next tooth to form the synthesizing meshing stiffness as shown in Figure 3. In the figure, the AB interval and CD interval represent the meshing interval of two pairs of teeth, while BC represents the meshing interval of one pair of teeth. At the moment of the transition of the meshing interval of one and two teeth, that is, the gear enters meshing or disengages in the meshing process; the synthesizing meshing stiffness of the gear will have a step change, which is an important characteristic of the synthesizing meshing stiffness of the gear.

2.1. Modeling of Time-Varying Mesh Stiffness of Tooth Flank Fracture. The crack propagation path of tooth flank fracture is shown in Figure 4. The main crack of tooth flank fracture first occurs inside the tooth, and one side of the main crack extends towards the tooth surface, while the other side of the main crack develops towards the root of the tooth opposite to the loaded tooth surface. Due to the high hardness of the tooth surface, the main crack extends toward the surface at a slower rate than toward the core. When the main crack extends to the extent that it affects the tooth stiffness, due to the action of loading, second cracks which almost parallel to the top of the tooth will occur. When the secondary crack meets the main crack, the particles will flake off in the area between the two cracks, and the tooth part here will be separated from the main body and lose transmission ability. With the continuous extension of the main crack to the tooth root of the core, when the main crack reaches the tooth

root surface, the tooth above the main crack is separated and the final tooth flank fracture is formed.

According to the tooth flank fracture propagation path above, the fault can be divided into four stages as shown in Figure 5.

In stage 1, the crack is located inside the gear tooth, and the crack is γ angle to the center line of the gear tooth. One side of the crack is located at the center line of the gear tooth and the other side does not extend to the surface of the loaded tooth. In stage 2, the crack extends to the surface of the loaded tooth, and a secondary crack parallel to the tip circle appears. In stage 3, the main crack continued to extend to the root of the tooth opposite the loaded tooth surface and intersected with the base circle. At the same time, the secondary crack intersected with the main crack, and the gray area between the main crack and the secondary crack is detached from the gear body. In stage 4, the main crack extends to the tooth root, and the gray part above the main crack is detached from the main body.

When analyzing the influence of cracks on the time-varying meshing stiffness, the Hertz stiffness, axial compression stiffness, and gear body stiffness are considered unchanged, while the fracture of the tooth flank only affects the bending stiffness and shear stiffness. Therefore, the area of the cross-section and the moment of inertia of the tooth are mainly considered. Due to different meshing positions, cracks have different effects on meshing stiffness, all of which are listed in Figure 6.

The formula for calculating the area of cross-section A_x and the moment of inertia I_x will be given as follows. The parameters not given are calculated in a manner consistent with the health gear.

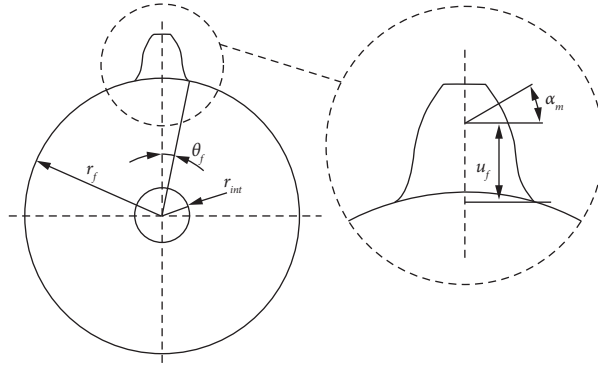


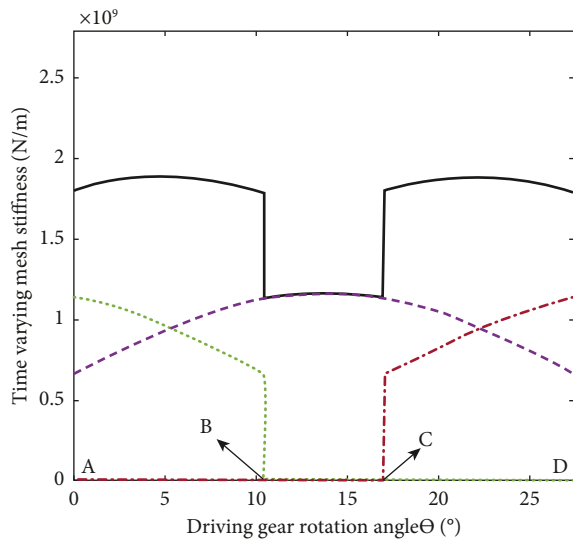
FIGURE 2: Gear body stiffness parameter diagram.

TABLE 1: Coefficients of gear body stiffness calculation.

	A	B	C	D	E	F
L^*	$-5.574e-5$	$-1.9986e-3$	$-2.3015e-4$	$4.7702e-3$	0.0271	6.8045
M^*	$60.111e-5$	$28.100e-3$	$-83.431e-4$	$-9.9256e-3$	0.1624	0.9086
P^*	$-50.952e-5$	$185.50e-3$	$0.0538e-4$	$53.300e-3$	0.2895	0.9236
Q^*	$-6.2042e-5$	$9.0889e-3$	$-4.0964e-4$	$7.8297e-3$	-0.1472	0.6904

TABLE 2: Gear parameters.

Gear symbol	Gear 1	Gear 2
Teeth number	21	57
Module (mm)		8
Mass (kg)	1.6	4.14
J (kg·m ²)	0.005	0.095
Bearing stiffness (N/m)		10^9
Bearing damping (N·s/m)		10^4
Mesh damping (N·s/rad)		10^4



- Synthetical stiffness
- - - Stiffness of the target tooth
- ... Stiffness of the previous pair of teeth
- · - Stiffness of the next pair of teeth

FIGURE 3: Composition of the synthesizing stiffness.

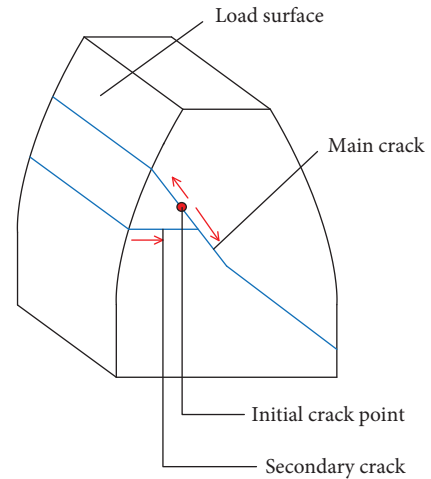


FIGURE 4: Crack propagation path of tooth flank fracture.

Stage 1-Case 1: meshing position d_1-d_2 ,

$$A_x = 2h_x L,$$

$$I_x = \frac{1}{12(2h_x)^3 L}. \tag{10}$$

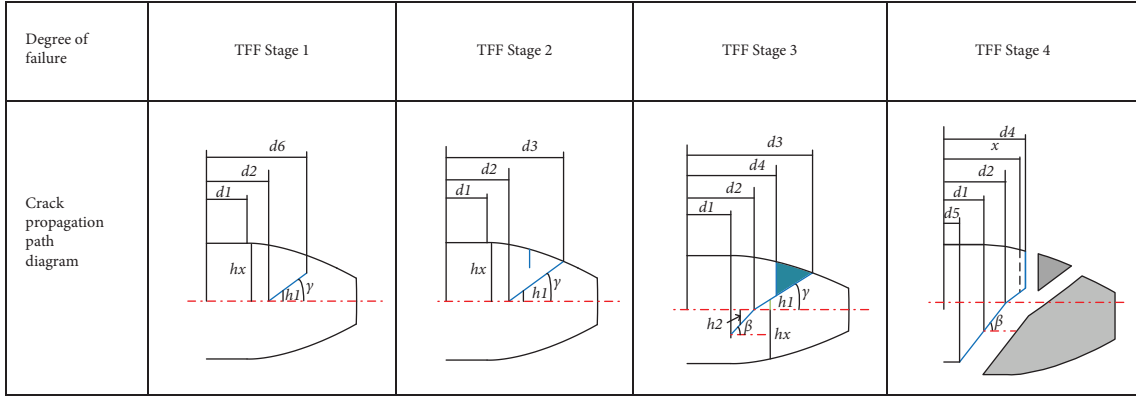


FIGURE 5: Fault degree diagram of tooth flank fracture.

Stage 1-Case 2: meshing position d_2 - d_6 ,

$$h_1 = (x - d_2)\tan \gamma,$$

$$A_x \begin{cases} 2h_x L, & \text{if } 0 < x < d_2, \\ (h_x - h_1)L, & \text{if } d_2 < x < d, \end{cases} \quad (11)$$

$$I_x \begin{cases} \frac{1}{12(2h_x)^3 L}, & \text{if } 0 < x < d_2, \\ \frac{1}{12(h_x - h_1)^3 L}, & \text{if } d_2 < x < d. \end{cases}$$

Stage 1-Case 3: meshing position d_3 -tip circle,

$$h_x = \begin{cases} R_b \sin \alpha_2, & \text{if } 0 < x < d_1, \\ R_b [(\alpha_2 - \alpha)\cos \alpha + \sin \alpha], & \text{if } d_1 < x < d, \end{cases}$$

$$h_1 = (x - d_2)\tan \gamma,$$

$$A_x \begin{cases} 2h_x L, & \text{if } 0 < x < d_2, \\ (h_x + h_1)L, & \text{if } d_2 < x < d_6, \\ 2h_x L, & \text{if } d_2 < x < d, \end{cases} \quad (12)$$

$$I_x \begin{cases} \frac{1}{12(2h_x)^3 L}, & \text{if } 0 < x < d_2, \\ \frac{1}{12(h_x + h_1)^3 L}, & \text{if } d_2 < x < d_6, \\ \frac{1}{12(2h_x)^3 L}, & \text{if } d_2 < x < d. \end{cases}$$

Stage 2-Case 1: meshing position d_1 - d_2 ,

$$A_x = 2h_x L,$$

$$I_x = \frac{1}{12(2h_x)^3 L} \quad (13)$$

Stage 2-Case 2: meshing position d_2 - d_3 ,

$$h_1 = (x - d_2)\tan \gamma,$$

$$A_x \begin{cases} 2h_x L, & \text{if } 0 < x < d_2, \\ (h_x - h_1)L, & \text{if } d_2 < x < d, \end{cases} \quad (14)$$

$$I_x \begin{cases} \frac{1}{12(2h_x)^3 L}, & \text{if } 0 < x < d_2, \\ \frac{1}{12(h_x - h_1)^3 L}, & \text{if } d_2 < x < d. \end{cases}$$

Stage 2-Case 3: meshing position d_3 -tip circle,

$$h_1 = (x - d_2)\tan \gamma,$$

$$A_x \begin{cases} 2h_x L, & \text{if } 0 < x < d_2, \\ (h_x + h_1)L, & \text{if } d_2 < x < d_3, \\ 2h_x L, & \text{if } d_3 < x < d, \end{cases} \quad (15)$$

$$I_x \begin{cases} \frac{1}{12(2h_x)^3 L}, & \text{if } 0 < x < d_2, \\ \frac{1}{12(h_x + h_1)^3 L}, & \text{if } d_2 < x < d_3, \\ \frac{1}{12(2h_x)^3 L}, & \text{if } d_3 < x < d. \end{cases}$$

Stage 3-Case 1: meshing position d_1 - d_2 ,

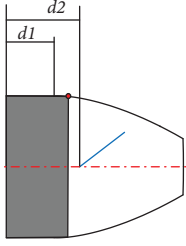
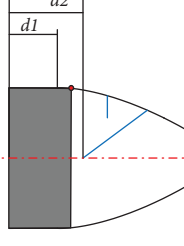
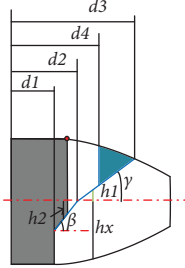
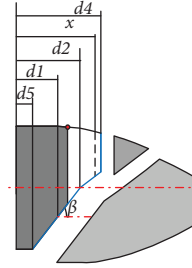
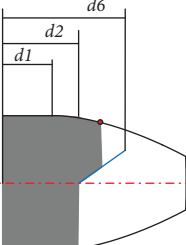
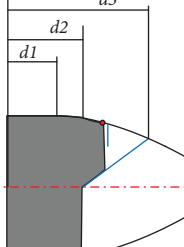
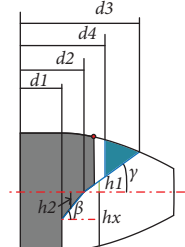
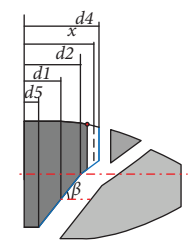
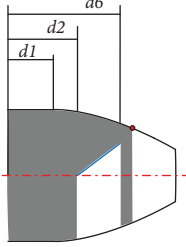
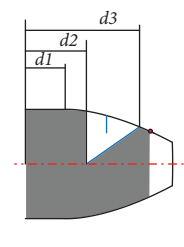
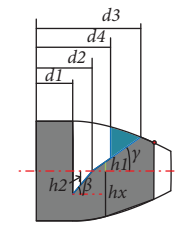
Degree of failure	TFF Stage 1	TFF Stage 2	TFF Stage 3	TFF Stage 4
meshing position: d_1-d_2	 <p>Stage 1-Case 1</p>	 <p>Stage 2-Case 1</p>	 <p>Stage 3-Case 1</p>	 <p>Stage 4-Case 1</p>
meshing position: d_2-d_4	 <p>Stage 1-Case 2</p>	 <p>Stage 2-Case 2</p>	 <p>Stage 3-Case 2</p>	 <p>Stage 4-Case 2</p>
meshing position: d_4-d_6			The gear is out of meshing and the stiffness becomes 0.	
meshing position: d_6-d_3			Stage 3-Case 3	The gear is out of meshing and the stiffness becomes 0.
meshing position: d_3 -tip circle	 <p>Stage 1-Case 3</p>	 <p>Stage 2-Case 3</p>	 <p>Stage 3-Case 4</p>	Stage 4-Case 3

FIGURE 6: Classification of different fault stages and meshing position of tooth flank fracture.

$$\begin{aligned}
 h_2 &= (d_2 - x)\tan\beta, \quad \text{if } d_1 < x < d, \\
 A_x &\begin{cases} 2h_x L, & \text{if } 0 < x < d_1, \\ (h_x + h_2)L, & \text{if } d_2 < x < d, \end{cases} \\
 I_x &\begin{cases} \frac{1}{12(2h_x)^3 L}, & \text{if } 0 < x < d_2, \\ \frac{1}{12(h_x + h_2)^3 L}, & \text{if } d_2 < x < d. \end{cases}
 \end{aligned} \tag{16}$$

Stage 3-Case 2: meshing position d_2 - d_4 ,

$$\begin{aligned}
 h_1 &= (x - d_2)\tan\gamma, \quad \text{if } d_2 < x < d, \\
 h_2 &= (d_2 - x)\tan\beta, \quad \text{if } d_1 < x < d_2, \\
 A_x &\begin{cases} 2h_x L, & \text{if } 0 < x < d_1, \\ (h_x + h_2)L, & \text{if } d_1 < x < d_2, \\ (h_x - h_1)L, & \text{if } d_2 < x < d, \end{cases} \\
 I_x &\begin{cases} \frac{1}{12(2h_x)^3 L}, & \text{if } 0 < x < d_1, \\ \frac{1}{12(h_x + h_2)^3 L}, & \text{if } d_1 < x < d_2, \\ \frac{1}{12(h_x - h_1)^3 L}, & \text{if } d_2 < x < d. \end{cases}
 \end{aligned} \tag{17}$$

Stage 3-Case 3: meshing position d_4 - d_3 .

As the secondary crack meets the main crack, this part of the gear tooth spalls off from the body, so when the meshing position is in this interval, the meshing stiffness of the gear is 0

Stage 3-Case 4: meshing position d_3 -tip circle,

$$\begin{aligned}
 h_1 &= (x - d_2)\tan\gamma, \quad \text{if } d_2 < x < d_3, \\
 h_2 &= (d_2 - x)\tan\beta, \quad \text{if } d_1 < x < d_2, \\
 A_x &\begin{cases} 2h_x L, & \text{if } 0 < x < d_1, \\ (h_x - h_2)L, & \text{if } d_1 < x < d_2, \\ (h_x + h_1)L, & \text{if } d_2 < x < d_3, \\ 2h_x L, & \text{if } d_3 < x < d, \end{cases} \\
 I_x &\begin{cases} \frac{1}{12(2h_x)^3 L}, & \text{if } 0 < x < d_1, \\ \frac{1}{12(h_x - h_2)^3 L}, & \text{if } d_1 < x < d_2, \\ \frac{1}{12(h_x + h_1)^3 L}, & \text{if } d_2 < x < d_3, \\ \frac{1}{12(2h_x)^3 L}, & \text{if } d_3 < x < d. \end{cases}
 \end{aligned} \tag{18}$$

Stage 4-Case 1: meshing position d_1 - d_2 ,

$$\begin{aligned}
 h_2 &= (d_2 - x)\tan\beta, \quad \text{if } d_5 < x < d, \\
 A_x &\begin{cases} 2h_x L, & \text{if } 0 < x < d_5, \\ (h_x + h_2)L, & \text{if } d_5 < x < d, \end{cases} \\
 I_x &\begin{cases} \frac{1}{12(2h_x)^3 L}, & \text{if } 0 < x < d_5, \\ \frac{1}{12(h_x + h_2)^3 L}, & \text{if } d_5 < x < d. \end{cases}
 \end{aligned} \tag{19}$$

Stage 4-Case 2: meshing position d_2 - d_4 ,

$$\begin{aligned}
h_1 &= (x - d_2)\tan \gamma, \quad \text{if } d_2 < x < d, \\
h_2 &= (d_2 - x)\tan \beta, \quad \text{if } d_5 < x < d_2, \\
A_x &\begin{cases} 2h_x L, & \text{if } 0 < x < d_5, \\ (h_x + h_2)L, & \text{if } d_5 < x < d_2, \\ (h_x - h_1)L, & \text{if } d_2 < x < d, \end{cases} \\
I_x &\begin{cases} \frac{1}{12(2h_x)^3 L}, & \text{if } 0 < x < d_5, \\ \frac{1}{12(h_x + h_2)^3 L}, & \text{if } d_5 < x < d_2, \\ \frac{1}{12(h_x - h_1)^3 L}, & \text{if } d_2 < x < d. \end{cases}
\end{aligned} \tag{20}$$

Stage 4-Case 3: meshing position d_4 -tip circle

Due to the fracture of the tooth, the stiffness of this part is considered 0

By combining the corrected bending stiffness and shear stiffness with unchanged Hertz stiffness, axial compression stiffness, and gear body stiffness, the time-varying meshing stiffness of the faulty tooth under tooth flank fracture is obtained, as shown in Figure 7(a). In stage 1, it is consistent with the healthy gear at the early stage of meshing. When the meshing point reaches position d_2 , the meshing stiffness of the gear begins to decline, and the declining value increases with the movement of the meshing point. In stage 2, at the early stage of meshing, it is consistent with the healthy gear. As the meshing point enters the crack region, the meshing stiffness of the gear gradually decreases. When the meshing point reaches the left side of the intersection point between the main crack and the load surface, the stiffness drops to the lowest point near zero; when the meshing point reaches the right side of the intersection point between the main crack and the load surface, the stiffness increases instantaneously. In stage 3, at the early stage of meshing, the stiffness of the gear gradually decreases compared with that of the healthy gear. When the meshing position is between d_4 and d_3 , the tooth between the main crack and the secondary crack detaches from the body, resulting in meshing failure. The stiffness of the gear decreases to 0, and when the meshing position is after d_3 , the stiffness differs greatly from that of healthy teeth. In stage 4, the stiffness of the faulty tooth is lower than that of the healthy tooth at the early stage of meshing, and when the meshing point reaches d_4 , the stiffness drops to 0.

Figure 7(b). The calculation results of the finite element method shall prevail, and the relative differences of the potential energy method are shown in Table 3. In the first, third, and fourth stages, the maximum differences calculated by the energy method are less than 10%, which verifies the accuracy of the time-varying meshing stiffness calculated by the potential energy method under tooth flank fracture. In stage 2, due to the left side of the intersection point between the main crack and the load surface, the tooth cross-section area and the moment of inertia are close to zero, which makes the differences in the calculation within 20% in the second stage.

The synthesizing meshing stiffness of gears considering the contact ratio is shown in Figure 8. The meshing stiffness of single tooth and double tooth appeared alternately, and the other variation trend is the same as that of a pair of teeth. Different from root fracture, the synthesizing meshing stiffness of tooth flank fracture does not completely break out of the meshing stage during the whole meshing process, indicating that the stiffness changes relatively slightly under this kind of fault.

2.2. Modeling of Time-Varying Mesh Stiffness of Tooth Interior Fatigue Fracture. The characteristics of tooth interior fatigue fracture are that the crack initiation point is inside the tooth, and the propagation path is almost parallel to the tip circle of the tooth. The propagation path of interior fatigue fracture is shown in Figure 9, and it can be divided into two stages as shown in Figure 10: the first stage is that the initial crack extends to both sides and the second stage is that one crack extends to the tooth surface and the other crack extends to intersect with the inner and opposite cracks of the gear tooth and the upper tooth segment breaks away from the gear tooth along the platform half tooth height.

Consistent with the fracture treatment of tooth flank, when the interior fatigue fracture occurs, it is considered that the Hertz stiffness, axial compression stiffness, and gear body stiffness remain unchanged, and the interior fatigue fracture failure only affects the bending stiffness and shear stiffness. Due to different meshing positions, stiffness calculation methods are also different, all of which are listed in Figure 11.

The calculation of cross-sectional area and moment of inertia in all cases is shown as follows:

Stage 1-Case 1: meshing position d_1 - d_7 ,

$$\begin{aligned}
A_x &= 2h_x L, \\
I_x &= \frac{1}{12(2h_x)^3 L}.
\end{aligned} \tag{21}$$

Stage 1-Case 2: meshing position d_1 - d_7 ,

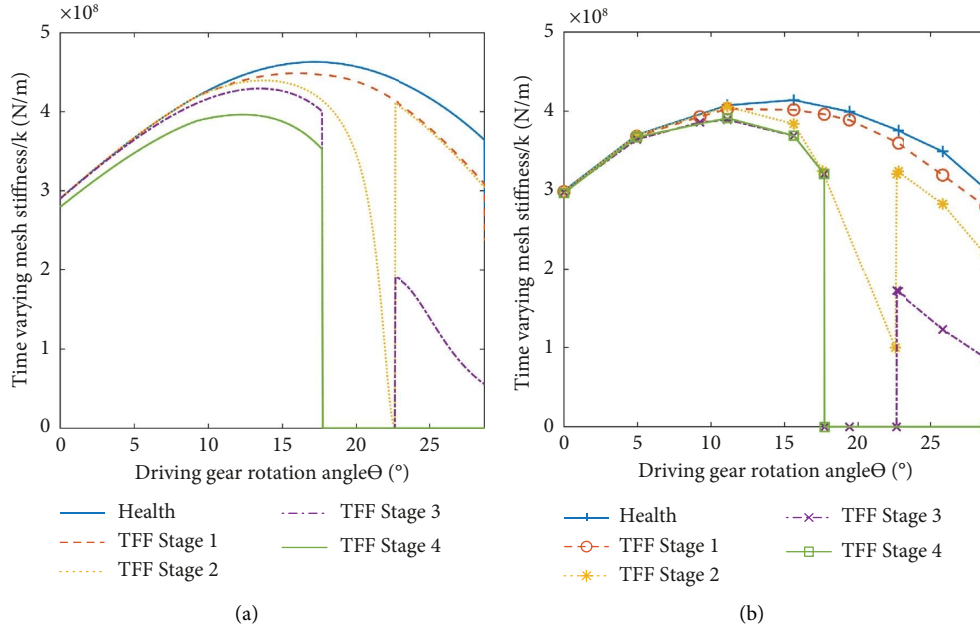


FIGURE 7: The stiffness of tooth with tooth flank fracture. (a) The result of PEM. (b) The result of FEM.

TABLE 3: Stiffness calculation comparison under tooth flank fracture.

Position	1 (%)	2 (%)	3 (%)	4 (%)	5 (%)	6 (%)	7 (%)	8 (%)
TFF stage 1	0.37	0.49	0.08	0.21	1.23	1.98	1.74	7.76
TFF stage 2	7.04	1.78	11.11	17.71	18.30	19.70	20.00	20.00
TFF stage 3	0.46	0.83	1.38	2.59	0%	0.06%	6.57	9.68
TFF stage 4	2.68	4.46	5.61	6.17	0	0	0	0

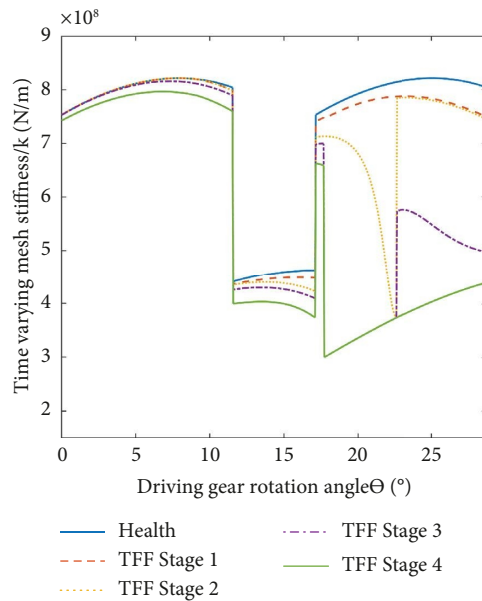


FIGURE 8: The synthesizing meshing stiffness of gears considering the contact ratio under tooth flank fracture.

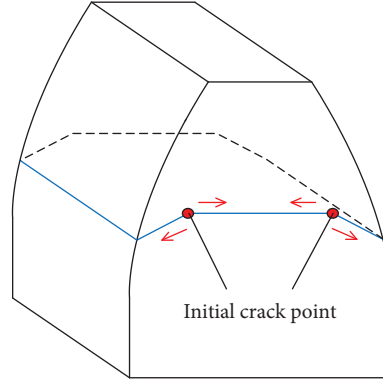


FIGURE 9: Propagation path of tooth interior fatigue fracture.

Degree of failure	TIFF Stage 1	TIFF Stage 2
Crack propagation path diagram		

FIGURE 10: Fault degree diagram of tooth interior fatigue fracture.

$$\begin{aligned}
 h_1 &= (d_8 - x)\tan \gamma, \\
 A_x &\begin{cases} 2h_x L, & \text{if } 0 < x < d_7, \\ (2h_x - 2h_1)L, & \text{if } d_7 < x < d, \end{cases} \\
 I_x &\begin{cases} \frac{1}{12(2h_x)^3 L}, & \text{if } 0 < x < d_7, \\ \frac{1}{12(2h_x - 2h_1)^3 L}, & \text{if } d_7 < x < d. \end{cases} \quad (22)
 \end{aligned}$$

Stage 1-Case 3: meshing position d_8 -tip circle,

$$\begin{aligned}
 A_x &\begin{cases} 2h_x L, & \text{if } 0 < x < d_7, \\ 2h_0 L, & \text{if } d_7 < x < d_8, \\ 2h_x L, & \text{if } d_8 < x < d, \end{cases} \\
 I_x &\begin{cases} \frac{1}{12(2h_x)^3 L}, & \text{if } 0 < x < d_7, \\ \frac{1}{12(2h_0)^3 L}, & \text{if } d_7 < x < d_8, \\ \frac{1}{12(2h_x)^3 L}, & \text{if } d_8 < x < d. \end{cases} \quad (23)
 \end{aligned}$$

Stage 2-Case 1: meshing position d_1 - d_9

At this time, the upper tooth segment disengages from the gear tooth along the platform of half tooth height, and the gear meshing position is before d_4 . Since the meshing position is consistent with the healthy teeth below, the stiffness remains unchanged

Stage 2-Case 2: meshing position d_9 -tip circle

Due to the tooth falling off, the gear is out of meshing and the stiffness is 0

The cross-section area and moment of inertia of the gear teeth, considering the first stage of tooth interior fatigue fracture failure, are put into the calculation formulas of bending stiffness and shear stiffness, and the corrected bending stiffness and shear stiffness are combined with the unchanged Hertz stiffness, axial compression stiffness, and gear body stiffness to obtain the time-varying mesh stiffness of the faulty tooth, as shown in Figure 12(a). It can be seen from the stiffness curve of the first stage that the stiffness of the fault tooth is the same as that of the healthy tooth at the early stage of meshing, and the stiffness decreases somewhat at the section where the crack is located. When the meshing interval is between d_8 and the tip circle of the tooth, the stiffness rises compared with the previous section but is still lower than that of the healthy tooth. In the stiffness curve of stage 2, it can be seen that the stiffness of the faulty tooth is consistent with that of the healthy tooth at the early stage of engagement and decreases to 0 when the tooth is removed from the position.

The tooth stiffness of the interior fatigue fracture fault by FEM is shown in Figure 12(b). The FEM results at the first stage of interior fatigue fracture are consistent with healthy stiffness at the early stage of meshing and a decrease in the crack zone. The stiffness increases at the late stage of meshing but is still lower than the healthy stiffness; in stage 2, the stiffness of the faulty tooth at the early stage of meshing is consistent with that of the healthy tooth, and the stiffness decreases to 0 after disengagement. The calculation results of the finite element method shall prevail, and the relative differences of the potential energy method are shown in Table 4. The difference in the result calculated by the potential energy method compared with the finite element

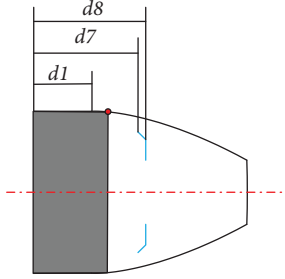
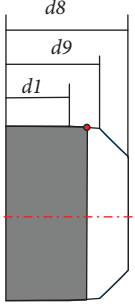
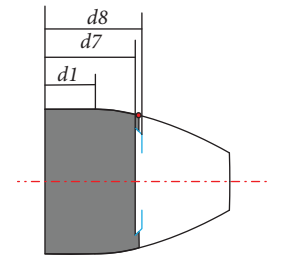
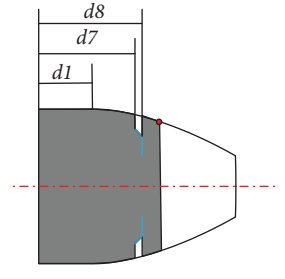
Degree of failure	Stage 1	Stage 2
meshing position: d_1-d_9		 Stage 1-Case 1
meshing position: d_9-d_7	Stage 1-Case 1	<p>The gear is out of meshing and the stiffness becomes 0.</p> <p>Stage 1-Case 2</p>
meshing position: d_7-d_8	 Stage 1-Case 2	
meshing position: d_8 -tip circle	 Stage 1-Case 3	

FIGURE 11: Classification of fault degree and meshing position of tooth interior fatigue fracture.

method is within 5%, which verifies the rationality of the energy method under tooth interior fatigue fracture.

The synthesizing stiffness of the gear after considering the contact ratio is shown in Figure 13. Since the synthesizing stiffness is formed by the superposition of the stiffness of the faulty gear and the healthy gear, the changing trend of

the synthesizing stiffness is consistent with that of the faulty tooth, and the difference between the stiffness of the gear and that of the healthy gear at each stage is consistent. In stage 2, the synthesizing mesh stiffness decreases to 0 at the lowest level, indicating that there is a stage of disengagement under the interior fatigue fracture fault set in this paper.

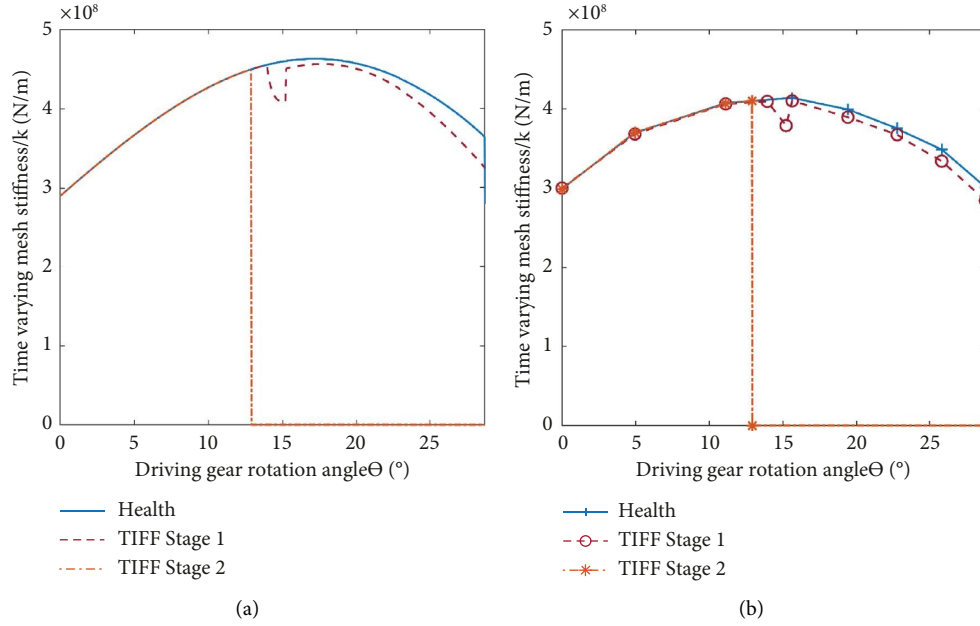


FIGURE 12: The tooth stiffness of tooth interior fatigue fracture failure. (a) The result of PEM. (b) The result of FEM.

TABLE 4: Stiffness calculation comparison under tooth interior fatigue fracture.

Position	1 (%)	2 (%)	3 (%)	4 (%)	5 (%)	6 (%)	7 (%)	8 (%)
TIFF stage 1	0.03	0.41	0.25	2.91	1.08	0.83	1.97	4.10
TIFF stage 2	0.01	0.41	0.20	0	0	0	0	0

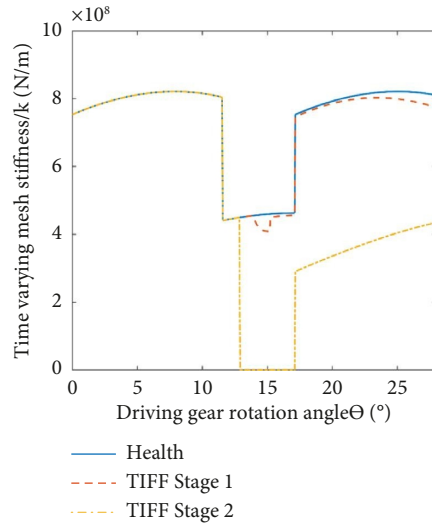


FIGURE 13: The synthesizing meshing stiffness of gears considering the contact ratio under tooth interior fatigue fracture.

3. Electromechanical Coupling Dynamic Model of Gear Set with Tooth Faults

The electromechanical coupling system model studied in this paper is the input system of the planetary gear differential speed

regulation system. Differential speed regulation of a planetary gear can be realized by the symmetrical arrangement of the fixed-axis gear system shown in Figure 14, which includes a three-phase inverter power supply, a three-phase induction motor, and a pair of spur gear with tooth faults.

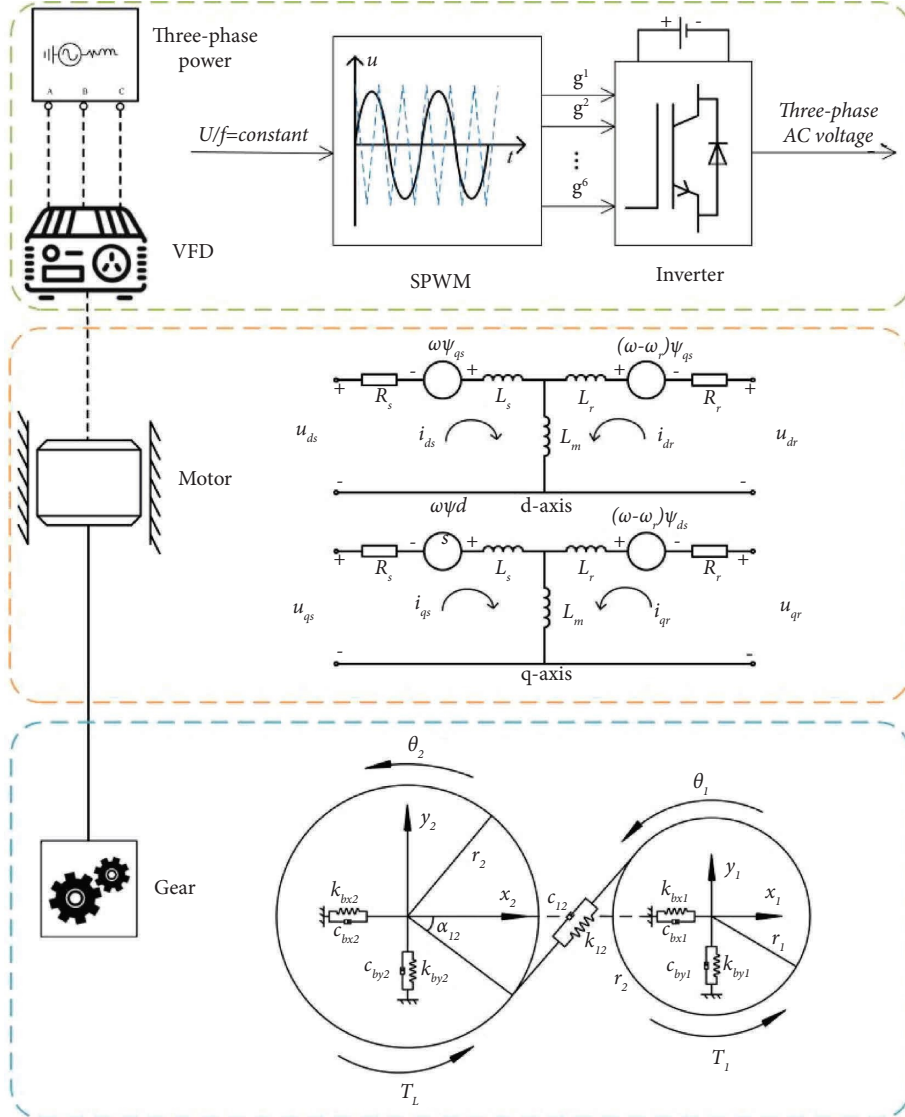


FIGURE 14: Diagram of the model of an electromechanical coupling system.

3.1. Inverter Model. The inverter power supply is selected for the motor, which can be used for variable-frequency drive. The schematic diagram is shown in Figure 14. The voltage and frequency of the power supply are calculated through the constant voltage frequency ratio control [26], and the signal generated by sinusoidal pulse-width modulation (SPWM) is used to drive the inverter composed of six power switching devices IGBT so that it generates the required three-phase voltage to drive the motor. This scheme can realize motor speed regulation.

3.2. Motor Model. The equivalent circuit model is used for motor modeling. Based on the Park transformation, the equivalent circuit model of the motor in the d - q coordinate system is established to describe the motor's motion. The equivalent circuit diagram is shown in Figure 14 [27]. The equivalent circuit model uses a set of homogeneous linear differential equations including

voltage equation, flux equation, and electromagnetic torque equation to describe the electromagnetic dynamics of the motor [28].

Corresponding voltage equations of the motor stator and rotor are shown in the following equation:

$$\begin{cases} u_{ds} = R_s i_{ds} + \frac{d}{dt} \psi_{ds} - \omega \psi_{qs}, \\ u_{qs} = R_s i_{qs} + \frac{d}{dt} \psi_{qs} + \omega \psi_{ds}, \\ u_{dr} = R_r i_{dr} + \frac{d}{dt} \psi_{dr} - (\omega - \omega_r) \psi_{qr}, \\ u_{qr} = R_r i_{qr} + \frac{d}{dt} \psi_{qr} + (\omega - \omega_r) \psi_{dr}, \end{cases} \quad (24)$$

where subscripts d and q , respectively, represent the axial-quantity d and axial quantity q , subscripts s and r , respectively, represent stator and rotor, u , i , and R , respectively, represent voltage, current, and resistance, ω , ω_r , respectively, represent the mechanical angular velocity of the rotor and electromagnetic angular velocity of the rotor, and ψ represent flux. Flux equations of the stator and rotor are

$$\begin{cases} \psi_{ds} = L_s i_{ds} + L_m i_{dr}, \\ \psi_{qs} = L_s i_{qs} + L_m i_{qr}, \\ \psi_{dr} = L_m i_{ds} + L_r i_{dr}, \\ \psi_{qr} = L_m i_{qs} + L_r i_{qr}, \end{cases} \quad (25)$$

where L_s and L_r are leakage inductance of stator and rotor windings, respectively, and L_m is electromagnetic mutual inductance. The generation of electromagnetic torque of a motor is essentially based on the interaction of magnetic flux and current, and its formula is

$$T_e = 1.5p(\psi_{ds}i_{qs} - \psi_{qs}i_{ds}), \quad (26)$$

where T_e is electromagnetic torque and p is the number of magnetic poles.

3.3. A Dynamic Model of Gear Set. The translation-torsional dynamics model of a spur gear pair as shown in Figure 14 is established. The supporting stiffness and damping, contact stiffness and damping, and time-varying meshing stiffness were considered in the governing equations as

$$\begin{cases} m_1 \ddot{x}_1 = (k_{12}\delta_{12} + c_{12}\dot{\delta}_{12})\sin\alpha_{12} - k_{bx1}x_1 - c_{bx1}\dot{x}_1, \\ m_1 \ddot{y}_1 = (k_{12}\delta_{12} + c_{12}\dot{\delta}_{12})\cos\alpha_{12} - k_{by1}y_1 - c_{by1}\dot{y}_1, \\ J_1 \ddot{\theta}_1 = T_1 - (k_{12}\delta_{12} + c_{12}\dot{\delta}_{12})r_1, \\ m_2 \ddot{x}_2 = -(k_{12}\delta_{12} + c_{12}\dot{\delta}_{12})\sin\alpha_{12} - k_{bx2}x_2 - c_{bx2}\dot{x}_2, \\ m_2 \ddot{y}_2 = -(k_{12}\delta_{12} + c_{12}\dot{\delta}_{12})\cos\alpha_{12} - k_{by2}y_2 - c_{by2}\dot{y}_2, \\ J_2 \ddot{\theta}_2 = T_L - (k_{12}\delta_{12} + c_{12}\dot{\delta}_{12})r_2. \end{cases} \quad (27)$$

The meshing deformation δ_{12} of the gear along the meshing line is shown in the following equation:

$$\delta_{12} = (x_2 - x_1)\sin\alpha_{12} + (y_2 - y_1)\cos\alpha_{12} + r_1\theta_1 + r_2\theta_2, \quad (28)$$

where J_i ($i=1, 2$) and m_i ($i=1, 2$) represent the moment of inertia and mass of each wheel. α_{12} represents the pressure angle of the gear. x_i ($i=1, 2$) and y_i ($i=1, 2$) represent the horizontal and vertical displacement of the gear. k_{bij} , c_{bij} ($i=x, y; j=1, 2$) represent the bearing stiffness and support damping in the horizontal and vertical directions. T_1 and T_L are, respectively, the input torques of gear 1 and gear 2. θ_i ($i=1, 2$) represents the angular displacement of the gear. r_1 and r_2 represent the pitch circle radius of the gear. k_{12} and c_{12} , respectively, represent the time-varying meshing stiffness and meshing damping, where the time-varying meshing stiffness can be either that of a healthy gear or that of a fault.

4. Simulation and Discussion

4.1. Vibration Characteristics of TRF, TFF, and TIFF at Different Fault Stages. The mechanical vibration during the evolution of the fault is simulated by the electromechanical coupling dynamics model, and the fault characteristics were analyzed in the time domain, frequency domain, and phase diagram, respectively. The motor and power supply parameters are listed in Table 5, which is calculated and chosen according to references [20, 21, 28] based on our model. In this paper, tooth root fracture (TRF), tooth flank fracture (TFF), and tooth interior fatigue fracture (TIFF) of gear fault characteristics will be studied.

To compare the vibration differences of TRF, TFF, and TIFF, a four-stage fault model of root fracture based on reference [29] is built, assuming that the root crack is a full-width penetrating crack. The crack propagation angle γ was set at 45° , the crack expanded inward in a straight line and then extended to the tooth root on the other side after reaching the center line. The fault degree was divided into four stages as shown in Figure 15.

Since the vibrations in the x direction and the y direction are similar, only the vibrations of the faulty gear in the y direction will be analyzed. The time domain diagram of vibration in the y direction is shown in Figure 16(a). It can be seen that for healthy gear teeth, the vibration fluctuates steadily within a small amplitude. With the deepening of the crack, a periodic pulse appears when the fault tooth engages, and the pulse amplitude increases with the deepening of the crack. When the fourth stage is reached, the root is completely broken, the vibration amplitude of the gear teeth reaches the maximum, and the other healthy teeth also lose their obvious periodicity.

The frequency domain diagram of vibration in the y direction is shown in Figure 16(b). Within the range of 0–3000 Hz, the meshing frequency of the healthy gear f_m and its frequency doubling are the main frequency components. In addition, the modulation frequencies $f_c - 3f_1$ and $f_c + 3f_1$ of the carrier frequency and the power frequency caused by the inverter are also obvious. With the increase of the crack, the meshing frequency and its amplitude of frequency doubling remain constant, and a very dense sideband appears in the vibration spectrum. The interval of the sideband is f_{r1} , the frequency corresponding to the fault pulse interval, which is also the rotation frequency of the gear shaft.

Figure 16(c) shows the enlarged image near the meshing frequency f_m . With the deepening of the fault, side bands such as $f_m \pm f_{r1}$, $f_m \pm 2f_{r1}$, and $f_m \pm 3f_{r1}$ can be found near the meshing frequency. With the deepening of the crack, side band components will gradually cover the other components.

Figure 16(d) shows the phase diagram of each fault stage. It can be seen that the phase range of the fault in the first stage is approximately the same as that of the healthy tooth. But from the second stage, the zone of instability begins to grow larger and reaches its maximum after the tooth is completely fractured.

TABLE 5: Motor system and power supply parameters.

Parameters	Value
Stator resistance R_s (Ω)	0.2761
Stator inductance L_s (H)	0.002191
Rotor resistance R_r (Ω)	0.1645
Rotor inductance L_r (H)	0.002191
Mutual inductance L_m (H)	0.07641
Friction factor F (N·m·s)	0.01771
Rated voltage U_N (V)	460
Rated frequency f_N (Hz)	60
Rated power P (kW)	14.9
Compensation voltage U_0 (V)	20
Triangular carrier amplitude U (V)	500
Triangular carrier frequency f_c	2500

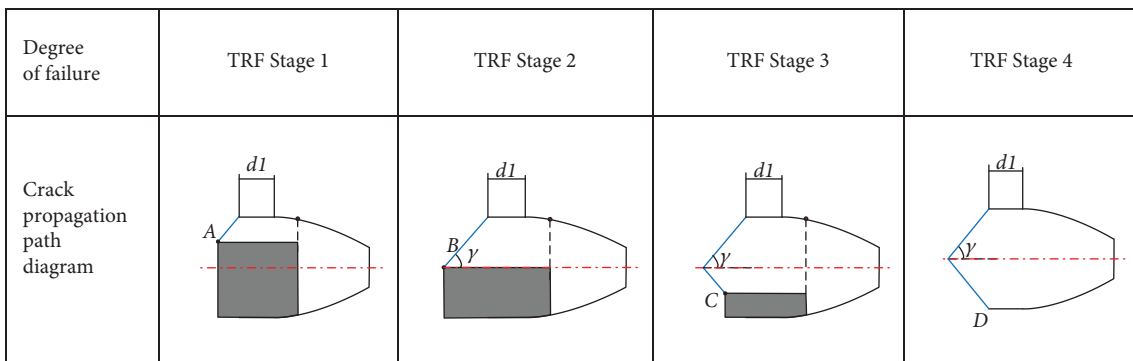


FIGURE 15: Fault degree diagram of tooth tooth fracture.

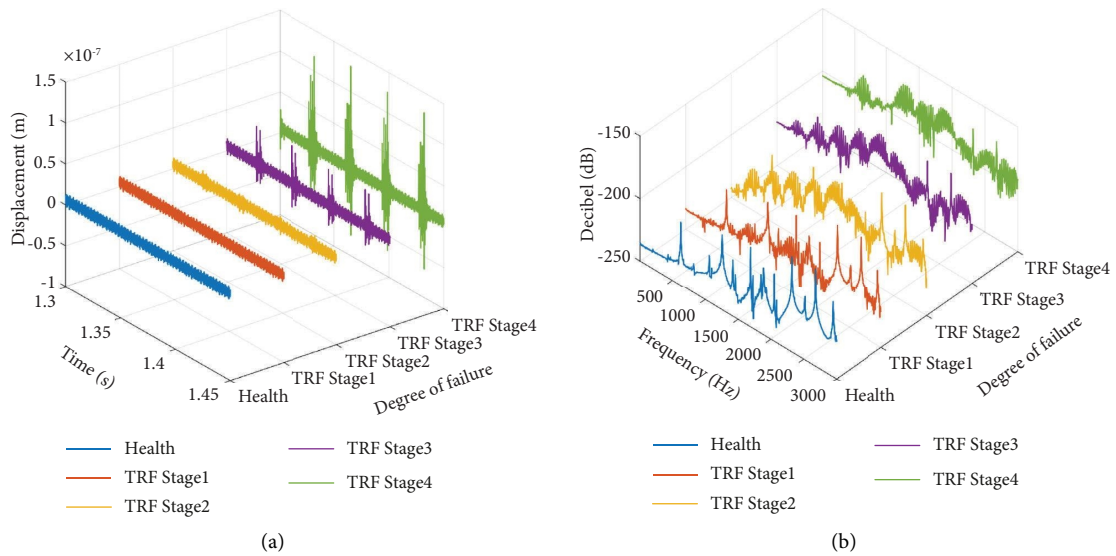


FIGURE 16: Continued.

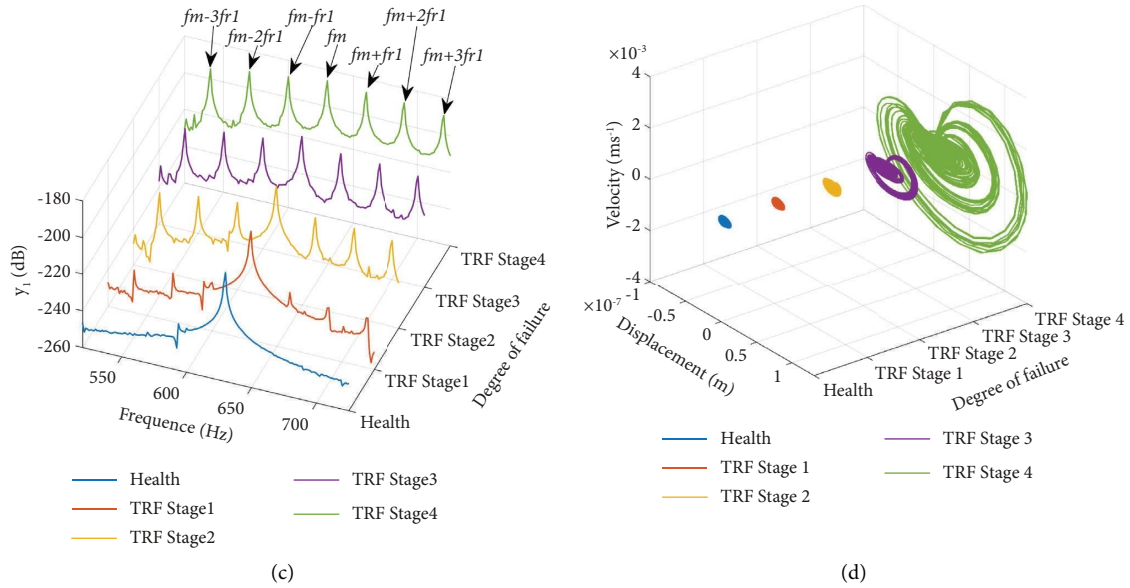


FIGURE 16: Vibration characteristic under tooth root fracture. (a) Time domain diagram. (b) Frequency domain diagram. (c) Partially enlarged figure in the frequency domain. (d) Phase diagram.

The time domain diagram of vibration in the y direction under tooth flank fracture is shown in Figure 17(a). Compared with the amplitude of tooth root fracture, the temporal translational vibration of gear under the stiffness excitation of tooth flank fracture has little change. This is because when tooth flank fracture occurs, the gear is always meshing due to the existence of the contact ratio. As the crack disengages below the circle of separation, the disengage moment exists.

The frequency domain diagram of vibration in the y direction is shown in Figure 17(b). Similar to tooth root fracture, within the range of 0–3000 Hz, the meshing frequency of healthy gear f_m and its frequency doubling is the main frequency components. In addition, the modulation frequencies $f_c - 3f_1$ and $f_c + 3f_1$ of the carrier frequency and the power frequency caused by the inverter are also obvious. With the increase of the crack degree, a very dense sideband appears in the vibration spectrum, corresponding to the frequency f_{r1} .

Figure 17(c) shows the enlarged image near the meshing frequency f_m . With the deepening of the fault, side bands such as $f_m \pm f_{r1}$, $f_m \pm 2f_{r1}$, and $f_m \pm 3f_{r1}$ can be found near the meshing frequency. Different from tooth root fracture, the meshing frequency is not covered by the sideband at the late stage of tooth flank fracture, and the meshing frequency and its frequency doubling can still be found, which also confirms the conclusion that the vibration change is a relatively small.

Figure 17(d) shows the phase diagram of four stages under tooth flank fracture. In the first stage, the phase diagram is almost unchanged, and the instability area gradually expands from the second stage, but the change of the phase diagram of tooth surface fracture is small compared with that of tooth root fracture.

The time domain diagram of vibration in the y direction under tooth interior fatigue fracture is shown in Figure 18(a). When the tooth interior fatigue fracture is in the first stage, that is, there is only an interior crack, the vibration amplitude increases periodically at the meshing position of the fault tooth, and there is little difference in the time domain as a whole. When the tooth interior fatigue fracture is in the second stage, the vibration amplitude of the fault tooth increases obviously, and the periodicity of each meshing tooth is irregular. This is because there is a disengagement stage with a stiffness of 0 in the synthetical meshing stiffness of the tooth, which leads to the intensification of vibration displacement.

The frequency domain diagram of vibration in the y direction is shown in Figure 18(b). Similar to the other two faults, in the range of 0–3000 Hz, the meshing frequency of the healthy gear and its frequency doubling, as well as the modulation frequency of the carrier frequency and the power frequency caused by the inverter is the main component.

The enlarged image near the meshing frequency f_m is shown in Figure 18(c). As the crack degree increases, the corresponding frequency f_{r1} appears in the vibration spectrum as a sideband. When the interior crack is in the second stage, the side band component increases, and the component exceeding the meshing frequency becomes the main component.

Figure 18(d) shows the phase diagram of two stages under tooth interior fatigue fracture. In the first stage, the phase diagram is also unchanged, however, in the second stage, the phase diagram instability area increases dramatically because the tooth break and fall away from the gear body.

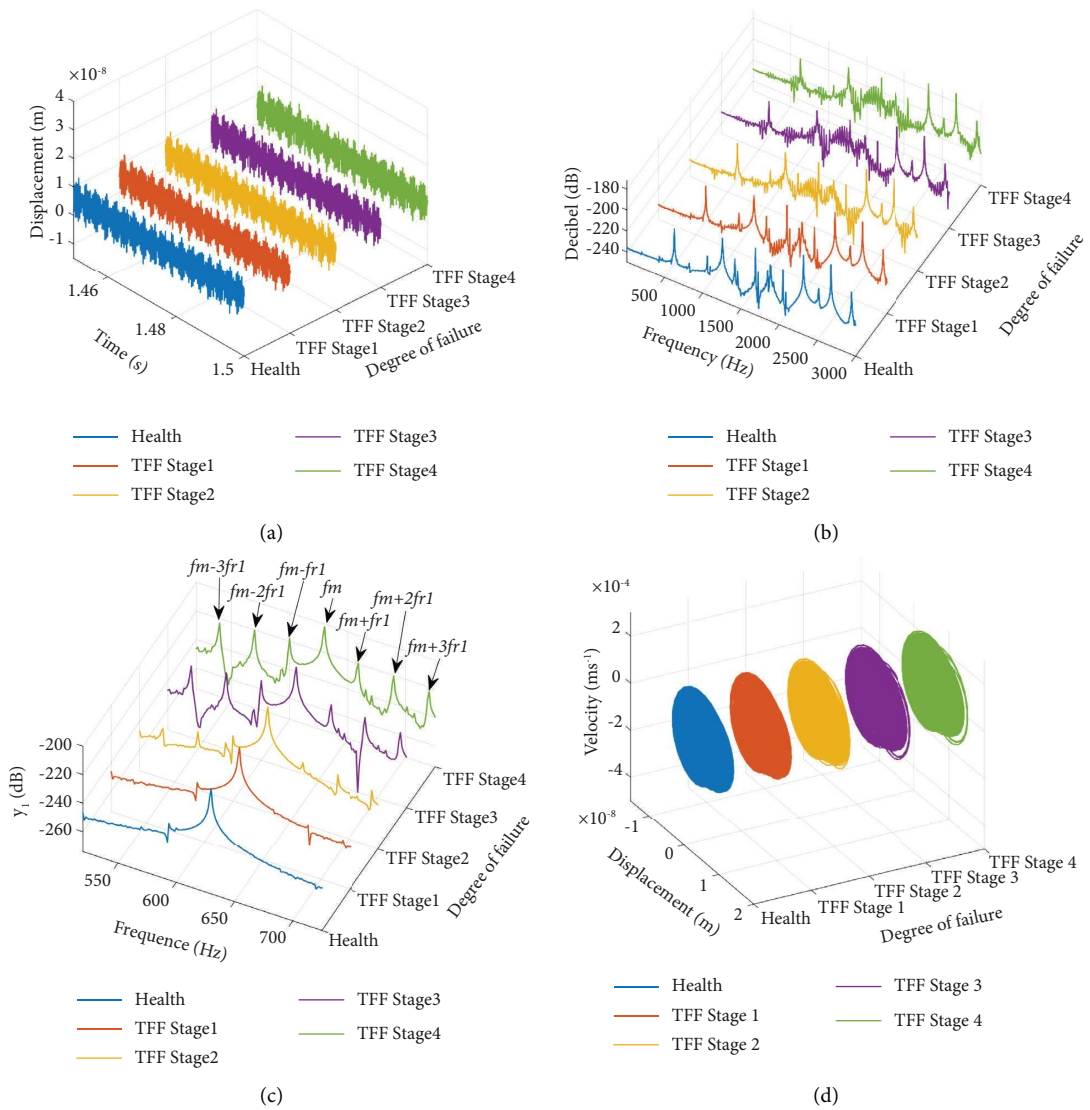


FIGURE 17: Vibration characteristic under tooth flank fracture. (a) Time domain vibration diagram. (b) Frequency domain diagram. (c) Partially enlarged figure in the frequency domain. (d) Phase diagram.

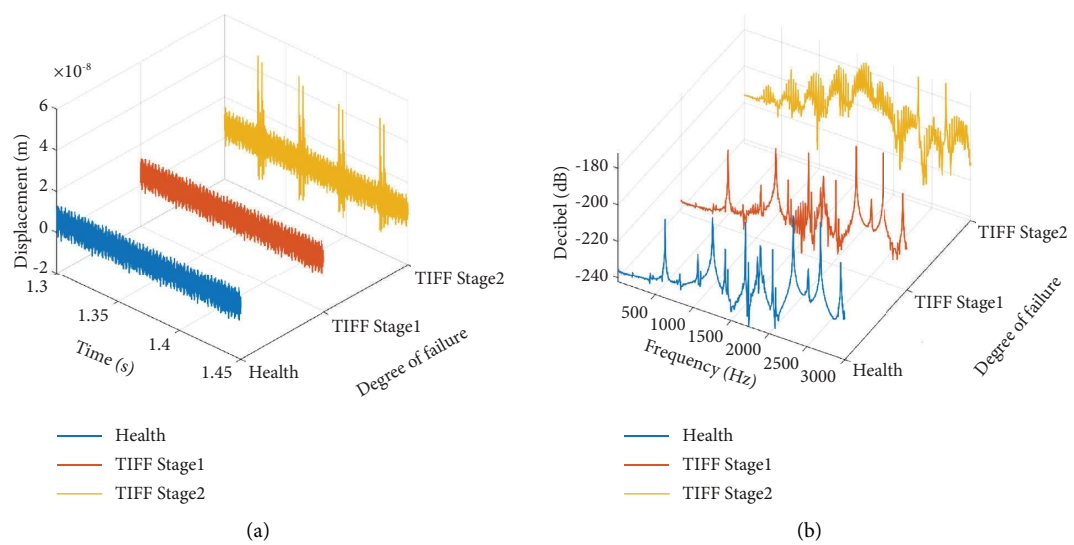


FIGURE 18: Continued.

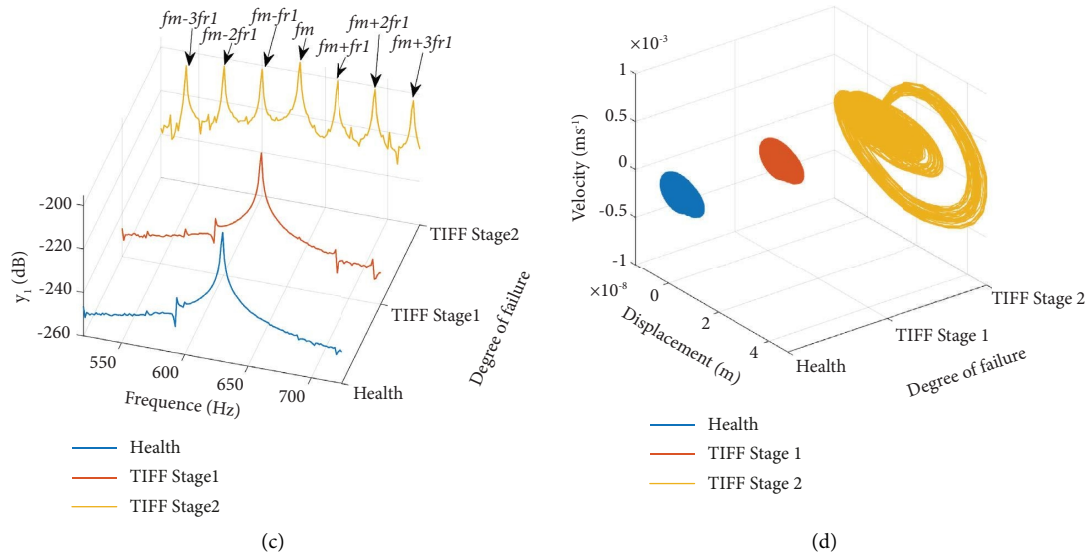


FIGURE 18: Vibration characteristic under tooth interior fatigue fracture. (a) Time domain vibration diagram. (b) Frequency domain diagram. (c) Partially enlarged figure in the frequency domain. (d) Phase diagram.

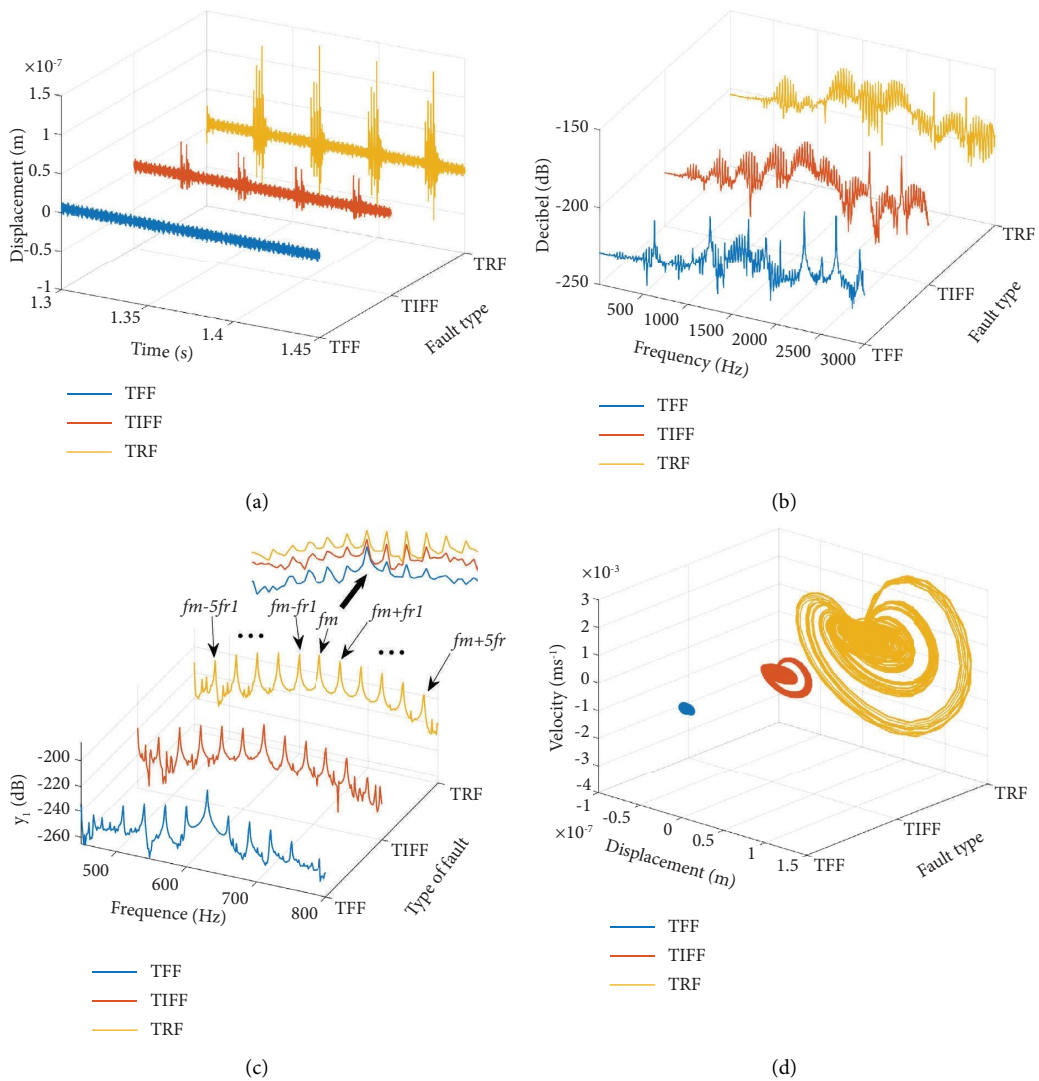


FIGURE 19: Comparison of fault characteristics under three kinds of fracture. (a) Time domain vibration diagram. (b) Frequency domain diagram. (c) Partially enlarged figure in the frequency domain. (d) Phase diagram.

4.2. *Fault Characteristic of TRF, TFF, and TIF under Complete Fracture.* When the three kinds of faults are in the final stage, that is, under complete fracture, the impact on the vibration of the system is as follows. Figure 19(a) shows the time domain diagram of gear translational vibration under three kinds of fracture faults. It can be seen that periodic pulses will be caused when the faulty tooth engage. The amplitude of the translational vibration pulse caused by root fracture is the largest, while that caused by tooth surface fracture is relatively small.

Figure 19(b) shows the frequency domain comparison of vibrations under three kinds of fracture faults. In addition to the meshing frequency and its frequency doubling, the sideband components near the meshing frequency have also become the main components. When the fault is tooth root fracture and tooth interior fatigue fracture, the amplitude of the sideband frequency has exceeded the meshing frequency amplitude. Figure 19(c) shows the enlarged image near the meshing frequency f_m . Only the meshing spectrum of the TFF fault can be found in the frequency diagram and has a smaller sideband range than the other two faults.

When the tooth flank fracture occurs, the meshing frequency can still be found in the frequency domain diagram, which is because the gear disengages after both root fracture and interior fatigue fracture happened. However, the gear will not be out of meshing under the tooth flank fracture fault. Therefore, in these three complete fracture faults, the tooth flank fracture can be distinguished from the other two faults by referring to the amplitude of the sideband near the meshing frequency and the amplitude of the meshing frequency.

Figure 19(d) shows the phase diagram corresponding to vibration in the y direction. The unstable region caused by tooth root fracture is larger than that caused by tooth interior fatigue fracture, and the unstable region caused by tooth flank fracture is minimum. From the vibration time domain and phase diagram of the three faulty gear systems, it can be seen that among the three faults, tooth root fracture has the greatest influence on the system, tooth flank fracture has the least influence, and tooth interior fatigue fracture is located between the two faults.

5. Conclusions

In this study, the time-varying mesh stiffness modeling of healthy gear, tooth flank fracture, and tooth interior fatigue fracture was established, and the electromechanical coupling system including a three-phase power supply considering an inverter, motor, and a pair of spur gear was also established to study the characteristics of the fault.

According to the generation mechanism of tooth flank fracture, the fault is divided into four symbolic stages, including only the interior main crack stage, the main crack extends to the loaded tooth surface and a secondary crack appearing, the main crack intersecting with the secondary crack, and the main crack extending to the opposite side of the loaded tooth surface. Tooth interior fatigue fracture can be divided into two stages: interior crack and complete fracture. Based on the stages and the different meshing

positions, the stiffness calculation modeling by the potential energy method was given in all cases, and the results were verified by the finite element method.

The electromechanical coupling model was established, and the vibration characteristics of tooth root fracture, tooth flank fracture, and tooth interior fatigue fracture were analyzed in time domain response, frequency domain response, and phase diagram. In the time domain, the amplitude of the vibration pulse caused by tooth root fracture is the largest, while that caused by tooth flank fracture is relatively small. In the phase diagram, the instability zone caused by tooth root fracture is the largest, the instability zone caused by tooth flank fracture is the smallest, and the tooth interior fatigue fracture is located between the two, which is corresponding to the vibration. In addition, in the initial stage of fault occurrence, the unstable region of the phase diagram hardly changes, and the occurrence of the fault can only be judged after the second stage by the changes in the unstable region of the three faults. In the frequency domain, after the occurrence of three kinds of faults, the extension degree of the side band is different. When the fault is tooth root fracture, the side band can be extended to $f_m + 5 f_{r1}$, which is the largest extension range of the three faults, so tooth root fracture can be distinguished from the other two faults by comparing the extent of side band extension. Future studies should set up scenarios that are closer to real conditions, such as considering the manufacturing errors of gears and the influence of noise signals on the analysis results.

Data Availability

No underlying data were collected or produced in this study.

Conflicts of Interest

The authors declare that they have no conflicts of interest that could have appeared to influence the work reported in this paper.

Acknowledgments

This study was supported by the National Natural Science Foundation of China (51775309) and the Key Technology Research and Development Project of Shandong Province (2019GGX104013).

References

- [1] O. D. Mohammed and M. Rantatalo, "Gear fault models and dynamics-based modelling for gear fault detection—A review," *Engineering Failure Analysis*, vol. 117, Article ID 104798, 2020.
- [2] M. MackAldener and M. Olsson, "Analysis of crack propagation during tooth interior fatigue fracture," *Engineering Fracture Mechanics*, vol. 69, no. 18, pp. 2147–2162, 2002.
- [3] I. Boiadjev, J. Witzig, T. Tobie, and K. Stahl, "Tooth flank fracture—basic principles and calculation model for a sub surface initiated fatigue failure mode of case hardened gears," in *Proceedings of the International Gear Conference*, pp. 26–28, Lyon, France, December, 2014.

- [4] D. C. Yang and J. Y. Lin, "Hertzian damping, tooth friction and bending elasticity in gear impact dynamics," *Journal of Mechanisms, Transmissions, and Automation in Design*, vol. 109, no. 2, pp. 189–196, 1987.
- [5] P. Sainsot and P. Velex, and O. Duverger, "Contribution of gear body to tooth deflections—a new bidimensional analytical formula," *Journal of Mechanical Design*, vol. 126, no. 4, pp. 748–752, 2004.
- [6] Z. G. Chen and Y. M. Shao, "Dynamic simulation of spur gear with tooth root crack propagating along tooth width and crack depth," *Engineering Failure Analysis*, vol. 18, no. 8, pp. 2149–2164, 2011.
- [7] X. Liang, M. J. Zuo, and M. Pandey, "Analytically evaluating the influence of crack on the mesh stiffness of a planetary gear set," *Mechanism and Machine Theory*, vol. 76, pp. 20–38, 2014.
- [8] O. D. Mohammed, M. Rantatalo, J. O. Aidanpää, and U. Kumar, "Vibration signal analysis for gear fault diagnosis with various crack progression scenarios," *Mechanical Systems and Signal Processing*, vol. 41, no. 1-2, pp. 176–195, 2013.
- [9] O. Doğan, C. Yuçe, and F. Karpat, "Effects of rim thickness and drive side pressure Angle on gear tooth root stress and fatigue crack propagation life," *Engineering Failure Analysis*, vol. 122, Article ID 105260, 2021.
- [10] X. Wang, Y. Yang, W. Wang, and W. Chi, "Simulating coupling behavior of spur gear meshing and fatigue crack propagation in tooth root," *International Journal of Fatigue*, vol. 134, Article ID 105381, 2020.
- [11] S. Wu, M. J. Zuo, and A. Parey, "Simulation of spur gear dynamics and estimation of fault growth," *Journal of Sound and Vibration*, vol. 317, no. 3-5, pp. 608–624, 2008.
- [12] T. Schneider, D. Müller, M. Seiler, T. Tobie, K. Stahl, and M. Kästner, "Phase-field modeling of fatigue crack growth during tooth flank fracture in case-hardened spur gears," *International Journal of Fatigue*, vol. 163, Article ID 107091, 2022.
- [13] B. Al, R. Patel, and P. Langlois, *Finite Element Analysis of Tooth Flank Fracture Using Boundary Conditions from LTCA*, Gear Technology, New Delhi, India, 2016.
- [14] Y. Yi, D. Qin, and C. Liu, "Investigation of electromechanical coupling vibration characteristics of an electric drive multi-stage gear system," *Mechanism and Machine Theory*, vol. 121, pp. 446–459, 2018.
- [15] W. Bai, D. Qin, Y. Wang, and T. Lim, "Dynamic characteristic of electromechanical coupling effects in motor-gear system," *Journal of Sound and Vibration*, vol. 423, pp. 50–64, 2018.
- [16] R. Shu, J. Wei, R. Tan, X. Wu, and B. Fu, "Investigation of dynamic and synchronization properties of a multi-motor driving system: theoretical analysis and experiment," *Mechanical Systems and Signal Processing*, vol. 153, no. 6, Article ID 107496, 2021.
- [17] A. Kahraman, "Natural modes of planetary gear trains," *Journal of Sound and Vibration*, vol. 173, no. 1, pp. 125–130, 1994.
- [18] J. Lin and R. G. Parker, "Analytical characterization of the unique properties of planetary gear free vibration," *Journal of Vibration and Acoustics*, vol. 121, no. 3, pp. 316–321, 1999.
- [19] F. Liu, L. Zhang, H. Jiang, J. Zhang, and J. Zhang, "Nonlinear dynamic analysis of two external excitations for the gear system using an original computational algorithm," *Mechanical Systems and Signal Processing*, vol. 144, Article ID 106823, 2020.
- [20] D. Wang, F. Yang, X. Jiang, S. Shi, and S. Ma, "Electromechanical coupling dynamic characteristics of differential speed regulation system considering inverter harmonics under variable operating conditions," *IEEE Access*, vol. 10, pp. 12057–12069, 2022.
- [21] L. Han, D. Wang, F. Yang, and W. He, "Vibration characteristics of the dual electric propulsion system of vessels under electromechanical coupling excitation," *Machines*, vol. 10, no. 6, p. 449, 2022.
- [22] O. D. Mohammed, M. Rantatalo, and J. O. Aidanpää, "Dynamic modelling of a one-stage spur gear system and vibration-based tooth crack detection analysis," *Mechanical Systems and Signal Processing*, vol. 54-55, pp. 293–305, 2015.
- [23] G. Liu, F. Liu, T. Ma, H. Jiang, C. Yang, and J. Zhang, "Dynamic analysis of spur gears system with dynamic force increment and velocity-dependent mesh stiffness," *Nonlinear Dynamics*, vol. 111, no. 15, pp. 13865–13887, 2023.
- [24] S. A. Abouel-seoud, E. S. Dyab, and M. S. Elmorsy, "Influence of tooth pitting and cracking on gear meshing stiffness and dynamic response of wind turbine gearbox," *International Journal of Science and Advanced Technology*, vol. 2, no. 3, pp. 151–165, 2012.
- [25] R. Ma and Y. Chen, "Research on the dynamic mechanism of the gear system with local crack and spalling failure," *Engineering Failure Analysis*, vol. 26, pp. 12–20, 2012.
- [26] J. I. Itoh, N. Nomura, and H. Ohsawa, "A comparison between V/f control and position-sensorless vector control for the permanent magnet synchronous motor," in *Proceedings of the Power Conversion Conference-Osaka 2002 (Cat. No. 02TH8579)*, vol. 3, pp. 1310–1315, Osaka, Japan, April, 2002.
- [27] A. Diaz, R. Saltares, C. Rodriguez, R. Nuñez, E. Ortiz-Rivera, and J. Gonzalez-Llorente, "Induction motor equivalent circuit for dynamic simulation," in *Proceedings of the 2009 IEEE International Electric Machines and Drives Conference*, pp. 858–863, IEEE, Miami, FL, USA, May, 2009.
- [28] B. Bilgin, J. Liang, M. V. Terzic et al., "Modeling and analysis of electric motors: state-of-the-art review," *IEEE Transactions on Transportation Electrification*, vol. 5, no. 3, pp. 602–617, 2019.
- [29] G. Li, *Research on Damage Modeling and Fault Diagnosis of Compound Planetary Gear Transmission System*, Shandong University, Jinan, China, 2017.